Calcium-Induced Alterations in Mitochondrial Morphology Quantified in Situ with Optical Scatter Imaging

Nada N. Boustany,* Rebekah Drezek,† and Nitish V. Thakor*
*Department of Biomedical Engineering, Johns Hopkins University, Baltimore, Maryland 21205, and †Department of Biomedical Engineering, Rice University, Houston, Texas 77005 USA

ABSTRACT Optical scatter imaging (OSI), a technique we developed recently, was used to measure the ratio of wide-to-narrow angle scatter (OSIR) within endothelial cells subjected to calcium overload (1.6 mM) after permeabilization by ionomycin. Within a few minutes of calcium overload, the mitochondria, which started as elongated organelles, rounded up into spherically shaped particles. This change in morphology was accompanied by a statistically significant 14% increase in OSIR in the cells' cytoplasm. Mitochondrial rounding and OSIR increase were suppressed by cyclosporin A (25 μM), implying that the observed geometrical and scattering changes were directly attributable to the mitochondrial permeability transition. The angular scattering properties of a long mitochondrion rounding up were approximated by numerical simulations of light scatter from an ellipsoid rounding up into a sphere. The simulations predicted a relative increase in OSIR comparable to that measured experimentally for the case where the shape transition takes place with little or no volume increase. The simulations also suggested that mitochondrial refractive index changes could not account for the OSIR changes observed. Our data show that changes in OSIR correlate with mitochondrial morphology change in situ. OSI provides a new tool for subcellular imaging and complements other microscopy methods, such as fluorescence.

INTRODUCTION

Alterations in mitochondrial morphology have been associated with mitochondrial metabolic state (Lehninger, 1959; Packer, 1960, 1967; Hackenbrock, 1966; Harris et al., 1969; Hunter et al., 1976; Halestrap, 1994; Territo et al., 2001) as well as ischemic and apoptotic cell death (Herdson et al., 1964; Pastorino et al., 1995; DiLisa et al., 1998; Vander-Heiden et al., 1997; Martinou et al., 1999; Bernardi et al., 2001; Mootha et al., 2001; Scorrano et al., 2002). Whereas change in mitochondrial morphology could be assessed by electron microscopy, dynamic studies of viable mitochondria typically use light scattering to study this organelle, whose size is close to the optical resolution of microscopes. Light scattering is sensitive to changes in the size and shape of particles with dimensions on the order of the wavelength. The light scattering measurement may be carried out either in a spectrophotometer with the mitochondria suspension contained in a regular cuvette or by flow cytometry. Measurements of light transmission or angular light scattering at 90° from a suspension of isolated mitochondria have long been correlated with the morphology of mitochondria in the orthodox and condensed states (Hackenbrock, 1966; Hunter et al., 1976). Since these early studies, light scattering has become the technique of choice to detect mitochondrial size change. Light scattering techniques have proved essential in studying the mitochondrial permeability transition (Hunter and Haworth, 1979; Bernardi et al., 1992; Bernardi, 1992; Petronilli et al., 1994; Hoek et al., 1995; Constantini et al., 1996; Scorrano et al., 1997; Kristal and Dubinsky, 1997). More recently, the same light scattering measurements were applied to the detection of mitochondrial morphology change during apoptosis using flow cytometry (Vander-Heiden et al., 1997) and by measuring changes either in 90° scatter or absorbance in a spectrophotometer (Zamzami et al., 1996; Jurgensmeier et al., 1998; Narita et al., 1998; Finucane et al., 1999). In these studies, mitochondria are usually isolated from the cell before the light scatter measurement can be carried out.

The goal of the present study is to show whether light scattering could be used to track relative changes in mitochondrial morphology within living cells. We use a recently developed optical scatter imaging (OSI) technique, which can track particle size in situ (Boustany et al., 2001). The OSI technique consists of a combination of light scatter spectroscopy and microscopy. Optical scatter images of monolayers of cells in culture are generated. These images directly encode the ratio of wide-to-narrow angle scatter within the full field of view. Although the cell cytoplasm may contain many several potential scatterers consisting of the different organelles, earlier results have shown that mitochondria should provide a very significant scattering signal (Beauvoit et al., 1994, 1995).

We had previously validated the OSI technique on polystyrene sphere suspensions, and shown that the measured scatter image ratio (OSIR) decreases monotonically with sphere diameter as predicted by theory (Boustany et al., 2001). Here, we validate OSI in a biological system. We use calcium injury as a model of mitochondrial size/shape change and demonstrate how the OSIR correlates with calcium-induced alterations in mitochondrial morphology in situ. Furthermore, we compare the scatter changes observed

Submitted January 16, 2002, and accepted for publication May 1, 2002.

Address reprint requests to Dr. Nada N. Boustany, Johns Hopkins University School of Medicine, Department of Biomedical Engineering, 720 Rutland Ave., Traylor 701, Baltimore, MD 21205. Tel.: 410-955-0077; Fax: 410-955-0549; E-mail: nnboustany@alum.mit.edu.

0006-3495/02/09/1691/10 $2.00

TABLE 1 Salt solutions used during calcium experiments

Solution number	NaCl (mM)	KCl (mM)	D-Glucose (mM)	Hepes (mM)	$CaCl_2$ (mM)	$MgCl_2$ (mM)	Ionomycin (μM)
1	135	5.9	10	12	1.5	1.2	0
2	135	5.9	10	12	0	10	20
3	135	5.9	10	12	1.6	0	0
4	135	5.9	10	12	0.8	0	0

All solutions had pH 7.4.

to theoretical light scattering predictions from ellipsoids and spheres. Both the experiments and the theoretical modeling are used to quantify the morphological response of mitochondria to calcium overload.

MATERIALS AND METHODS

Cell culture

Bovine aortic endothelial cells (Clonetics, Walkersville, MD) were cultured on glass coverslips in Dulbecco's modified Eagle's medium (DMEM) supplemented with 10% fetal bovine serum (FBS), 2 mM L-glutamine, 20 U/ml heparin, 0.012 mg/ml bovine brain extract, 40 U/ml penicillin, and 40 μg/ml streptomycin. DMEM, FBS, L-glutamine, penicillin, and streptomycin were from Life Technologies (Rockville, MD). Heparin was from Sigma Chemical Co. (St. Louis, MO). Bovine brain extract was from Clonetics (Walkersville, MD). The cells were kept in culture at 37°C in a 5% CO_2 in air atmosphere.

Calcium experiments

Each coverslip with attached live cells was mounted by means of a steel plate onto the stage of the inverted microscope. Just before mounting onto the microscope's stage, the growth medium was replaced with a salt solution containing calcium and magnesium (solution 1 in Table 1). While still on the microscope stage, the cell membranes were permeabilized for 15 min in a calcium-free salt solution (solution 2 in Table 1) supplemented with 20 μM of the calcium ionophore, ionomycin (Calbiochem, San Diego, CA). After permeabilization, solution 2 was replaced by a final salt solution containing calcium, which can now pass through the cell membranes. Two different calcium concentrations (solution 3 or 4 in Table 1) were used after permeabilization to probe the response of mitochondria to high calcium. In the data presented, solution 4 (0.8 mM $CaCl_2$) was used for the cell depicted in Figs. 2 and 3, whereas solution 3 (1.6 mM $CaCl_2$) was used for the cells discussed in Figs. 4 and 5. To assess whether the mitochondrial changes observed were caused by the mitochondrial permeability transition, cyclosporin A (CsA) was used to block the mitochondrial permeability transition, (Broekemeier et al., 1989; Zoratti and Szabo, 1995). In this case, 25 μM cyclosporine (Novartis, East Hanover, NJ) was added to all solutions, before, during, and after ionomycin permeabilization. All calcium experiments were conducted at room temperature.

In selected cases, the live cells were pre-labeled with the fluorescent mitochondrial probe Mitotracker Green (Molecular Probes, Eugene, OR) to visualize specifically the mitochondria. For this, the cells were incubated for 45 min in growth medium supplemented with 100 nM Mitotracker Green before transferring the coverslips to the microscopy setup. Mitotracker labeling was done at 37°C in the 5% CO_2 in air atmosphere.

Apparatus and data acquisition

The OSI technique was described previously in detail (Boustany et al., 2001). Fig. 1 shows the microscopy setup. The specimens were mounted on the stage of an inverted microscope (Nikon, Eclipse T300, Melville NY), which was also fitted with epifluorescence and differential interference contrast (DIC) imaging capabilities. The microscope condenser was adjusted to central Kohler illumination, with a condenser numerical aperture (NA) of 0.03 (condenser front aperture closed). For illumination, light from the microscope's halogen lamp was filtered to yield an incident red beam, $\lambda = 630 \pm 5$ nm. The images were collected with a $\times$60 oil immersion objective, NA = 1.4, and displayed on a charge coupled device camera (Sensicam, Cooke Corp., Auburn Hills, MI). In a Fourier plane conjugate to the back focal plane of the objective, a beam stop was placed in the center of an iris with variable diameter. As the inset in Fig. 1 shows, the variable iris collected light scattered within a solid angle, bound by $2° < \theta < 10°$ for low NA, and $2° < \theta < 67°$ for high NA. The diameter of the beam block (0.5 mm), the smallest iris diameter, and the NA of the microscope objective defined the angles 2°, 10°, and 67°, respectively. The angles 2° and 10° were measured from the diffraction pattern of a grid of lines with spacing $a = 10$ μm.

For each specimen studied, two sequential dark-field images, collected 20–30 s apart, were acquired at high and low NA by manually adjusting the diameter of the variable iris. A solvent sample consisting of the salt solution in which the sample was prepared served to provide the background scatter signal due to the microscope optics. This background signal was subtracted from each image. The background-subtracted dark-field images were binned into pixels that, depending on the final magnification, corresponded to regions in the object between 2×2 μm^2 and 2.5×2.5 μm^2. The OSIR was then measured at each pixel bin by dividing the background-subtracted high NA image by the background-subtracted low NA image. Given the aperture settings used, OSIR can be defined as:

$$\mathrm{OSIR} = \frac{\int_{\phi=0}^{360°}\int_{\theta=2°}^{67°} F(\theta,\phi)\sin\theta\, d\theta\, d\phi}{\int_{\phi=0}^{360°}\int_{\theta=2°}^{10°} F(\theta,\phi)\sin\theta\, d\theta\, d\phi} \quad (1)$$

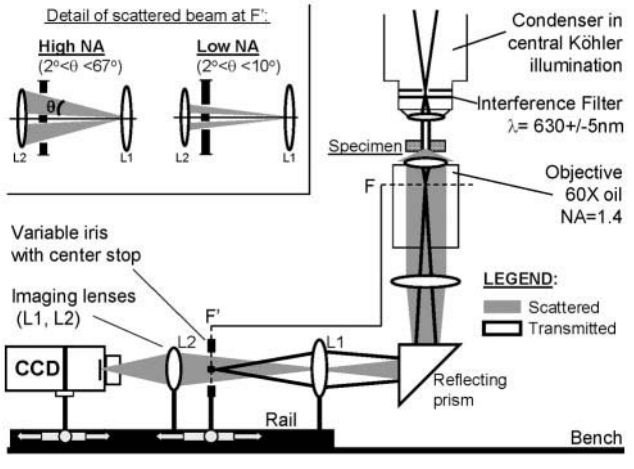

FIGURE 1 OSI setup. F represents the objective's back focal plane. F and F′ are conjugate Fourier planes. The scattered light (gray beam) is used to image the specimen on the CCD, while the transmitted light (black ray traces) is blocked at F′. The inset shows the scattered angles passed at the high and low numerical aperture (NA) settings. Sequential high and low images were collected by manual adjustment of the variable iris diameter. Each high and low NA image pair was collected within 20–30 s. (This figure was originally published in Optics Letters, 26:1063–1065 (2001), and is here reprinted with permission from the Optical Society of America.)

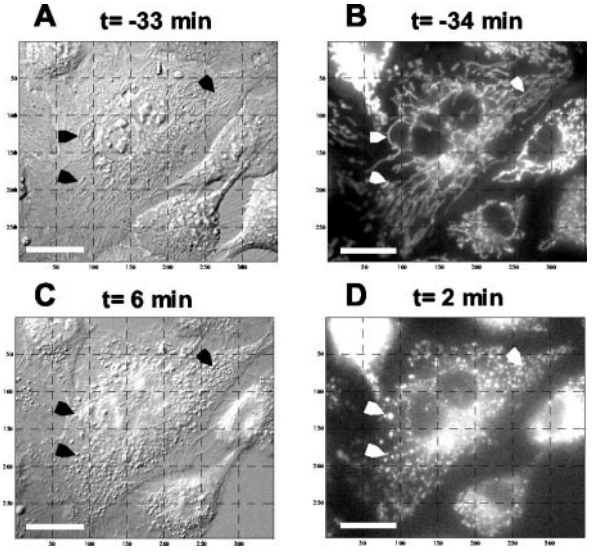

FIGURE 2 Mitochondria (*arrows*) within an endothelial cell before (*A* and *B*) and after (*C* and *D*) calcium injury. Calcium (0.8 mM) was added at $t = 0$ after permeabilization by ionomycin (20 μM). (*A* and *C*) DIC; (*B* and *D*) Mitochondrial fluorescence after labeling with Mitotracker Green. Scale bar, 20 μm.

where $F(\theta, \phi)$ gives the intensity of the light scattered in a given direction defined by the angles θ and ϕ. θ is the angle between the scatter direction and the direction of propagation of the incident light, and ϕ is the azimuthal angle of scatter.

Light scatter simulations

Simulations of light scattering from spheres and ellipsoids were carried out utilizing the finite-difference time-domain technique (Dunn et al., 1996; Drezek et al., 1999). These simulations were used to calculate the scatter intensity function $F(\theta, \phi)$ in Eq. 1. The scatter ratio, OSIR, was calculated after numerical integration of the scatter intensity function $F(\theta, \phi)$ according to Eq. 1. In these simulations, the incident light was naturally polarized, and the incident wavelength was $\lambda = 630$ nm. The cytoplasm refractive index was 1.35. The initial mitochondria refractive index was 1.4.

RESULTS

Effect of calcium treatment on mitochondria and light scattering

In Fig. 2, differential interference contrast (Fig. 2, *A* and *C*) and fluorescence (Fig. 2, *B* and *D*) images depict the sudden change in the shape of mitochondria within a few minutes of calcium overload. Mitotracker Green, which was used to stain the mitochondria, shows a fluorescent pattern in Fig. 2 *B* consistent with other studies of endothelial cell mitochondria stained with functional dyes such as fura 2 and rhodamine 123 (Steinberg et al., 1987), rhodamine 6G (Siemens et al., 1982), or a fluorescent antibody toward a mitochondrial protein (Lewis et al., 1991). The mitochondria (arrows), which are the elongated organelles before calcium injury (Fig. 2, *A* and *B*) round up in response to the sudden increase in cytoplasmic calcium (Fig. 2, *C* and *D*). Fig. 3 shows the dark-field images and ratiometric scatter images for the cell depicted in Fig. 2, before and after the calcium insult (upper and lower panels, respectively). Fig. 3, *A* and *D*, shows the dark-field images collected with the high NA setting of the variable iris before (Fig. 3 *A*) and after (Fig. 3 *D*) the calcium overload. Fig. 3, *B* and *E*, shows the dark-field images collected with the low NA setting of the iris. In

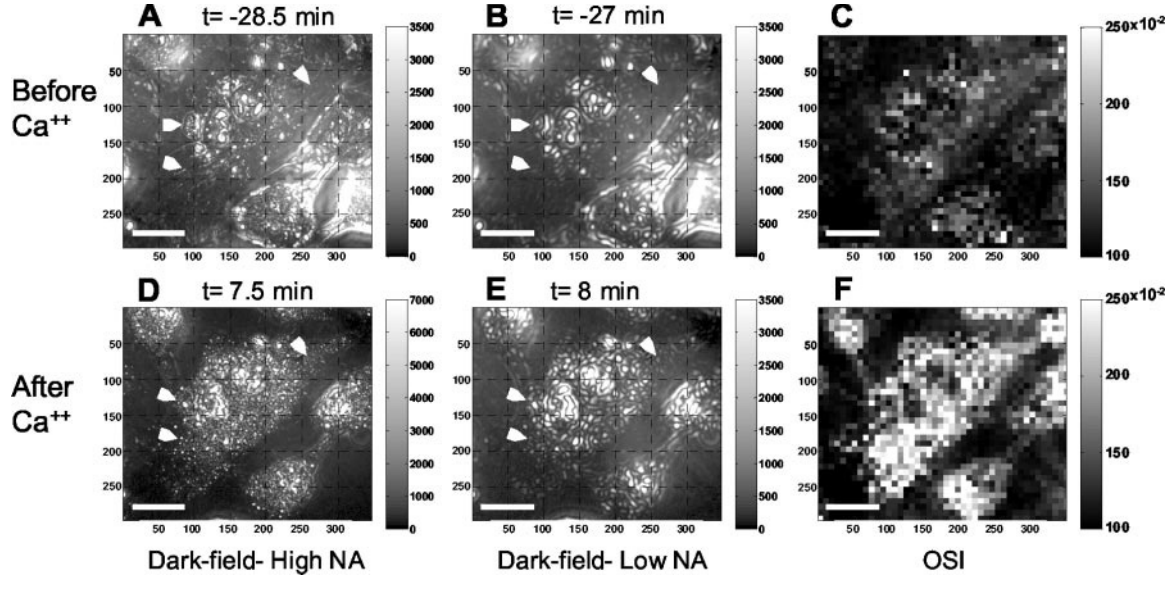

FIGURE 3 Dark-field and ratiometric optical scatter images (OSI) before (*upper panels*) and after (*lower panels*) calcium injury for the endothelial cell previously depicted in Fig. 2. Calcium (0.8 mM) was added at $t = 0$ after permeabilization by ionomycin (20 μM). (*A* and *D*) Dark-field images collected at high numerical aperture (NA); (*B* and *E*) Dark-field images collected at low NA; (*C* and *F*) Ratiometric optical scatter images with $C = A/B$ and $F = D/E$ after binning the background-subtracted dark-field images. In *C* and *F*, the intensity (gray scale) corresponds to the OSIR measured at each pixel bin (see Eq. 1). Scale bar, 20 μm. Arrows point to mitochondria (same *arrows* as in Fig. 2).

these dark-field images, the transmitted light has been blocked out by the beam stop in the center of the variable iris (see Fig. 1), and the intensity is directly proportional to the intensity of the light scattered by the particles (organelles) within the cell. By comparing Fig. 3, *A* and *D*, with Fig. 2, *B* and *D*, we find that a considerable number of scatterers within the cytoplasm of endothelial cells correspond to mitochondria (arrows in both Figs. 2 and 3).

In these dark-field images, certain scattering effects can also be observed. For example, one would expect from scatter theory that the larger a particle, and the larger the difference between its refractive index and that of the surrounding medium, the larger its scattering cross section, and the brighter it will appear in this central dark-field imaging configuration. Moreover, the ratio of wide- to narrow-angle scatter will generally decrease with increasing particle size. These scattering effects can be observed in Fig. 3, *A* and *B*, keeping in mind that index differences among organelles are relatively small. For example, the nucleoli (e.g., particle at grid coordinate 110 (row) and 140 (column) in Fig. 3 *A*) appear brighter than the smaller organelles in the cytoplasm because of their larger size. Moreover, the difference between the nucleoli and organelle intensity is accentuated at low NA (Fig. 3 *B*). Larger particles are expected to have a more forward-directed scatter. Thus, the intensity of small organelles becomes more significantly attenuated than that of larger organelles when the iris diameter is reduced at F′ in the optical setup (see Fig. 1).

The OSI technique consists of taking the ratio of the high to low NA image after binning, which ensures that each pixel bin includes most of the scatter intensity from at least one particle (see Materials and Methods). The ratiometric scatter images are shown in Fig. 3, *C* and *F*. The change in the morphology of the mitochondria previously shown in Fig. 2 is accompanied by a significant intensity increase in the optical scatter image (Fig. 3, *C*→*F*). The subcellular regions exhibiting the largest change in OSIR correspond to the regions in which the mitochondrial shape changes result in the most pronounced changes in angular scatter properties. These regions may not always correspond to the regions of most intense Mitotracker fluorescence signal, which itself does not depend on angular scatter properties but rather on mitochondrial concentration and retention of Mitotracker in the mitochondrial matrix. The OSIR increase depicted in Fig. 3 was reproducible. After segmenting the images, the OSIR was averaged over the cytoplasm of each tested cell, excluding the nucleus. The mean OSIR values per cell thus generated were subsequently normalized, then averaged and plotted in Fig. 4 (filled circles) for all cells ($n = 70$) subjected to calcium injury. The average OSIR values before and a few minutes after calcium addition are listed in Table 2. The mean OSIR increased by 14% and went from 1.47 to 1.68 upon calcium addition. Adding the mitochondrial permeability transition inhibitor CsA resulted in no significant scatter ratio change (Fig. 4, open squares, $n = 64$) and no mitochondrial rounding (an illustrative example is shown in Fig. 5). The suppression of OSIR increase by CsA shows that mitochondrial changes resulting from the permeability transition fully account for the scatter changes observed. Using solution 4 (0.8 mM calcium) instead of solution 3 (1.6 mM calcium) after permeabilization (see Table 1) resulted in 63% of the cells exhibiting no mitochondrial changes at 0.8 mM calcium, compared with 6% at 1.6 mM. However, at either of the two calcium concentrations, whenever the cells responded to the calcium insult, they exhibited the same mitochondrial and OSIR changes.

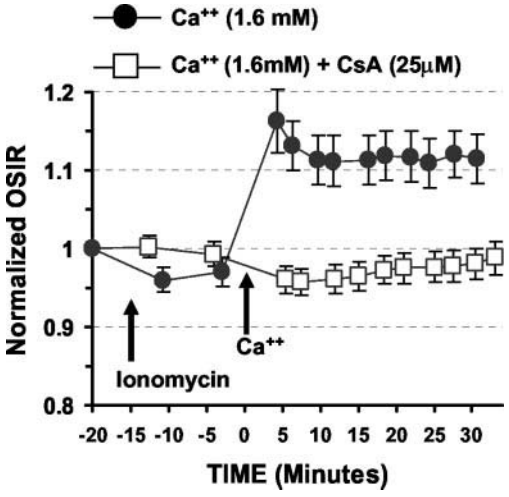

FIGURE 4 Average OSIR as a function of time. After collecting the initial data point in the control salt solution (solution 1 in Table 1), the cells were permeabilized for 15 min with ionomycin (20 μM) in a calcium-free solution (solution 2 in Table 1). For each tested cell, the OSIR was averaged over the cytoplasm, excluding the nucleus, and normalized to the initial OSIR value before permeabilization. The normalized mean OSIR values per cell thus generated were subsequently averaged and plotted here. The error bars represent the 95% confidence interval of the mean. ●, cells ($n = 70$) subjected to calcium injury (1.6 mM solution 3 in Table 1) at $t = 0$; □, cells ($n = 64$) subjected to calcium injury (1.6 mM) in the presence of 25 μM CsA. In this case, all solutions (1, 2, and 3) were supplemented with 25 μM CsA.

TABLE 2 OSIR averaged over the cytoplasms of all cells tested

Ca^{++} (1.6 mM), 70 cells tested		Ca^{++} (1.6 mM) + CsA (25 μM), 64 cells tested	
OSIR ($t < 0$)	OSIR ($t = 4$ min)	OSIR ($t < 0$)	OSIR ($t = 6$ min)
1.47 (0.05)	1.68 (0.06) $p < 10^{-7}$	1.36 (0.05)	1.31 (0.05) $p < 0.15$

Values are mean (95% confidence interval of the mean). Calcium was added at $t = 0$. The p values indicate the probability of correlation between the two data sets, before and after calcium injury, as calculated from a two-tailed Student's t-test with equal distributions.

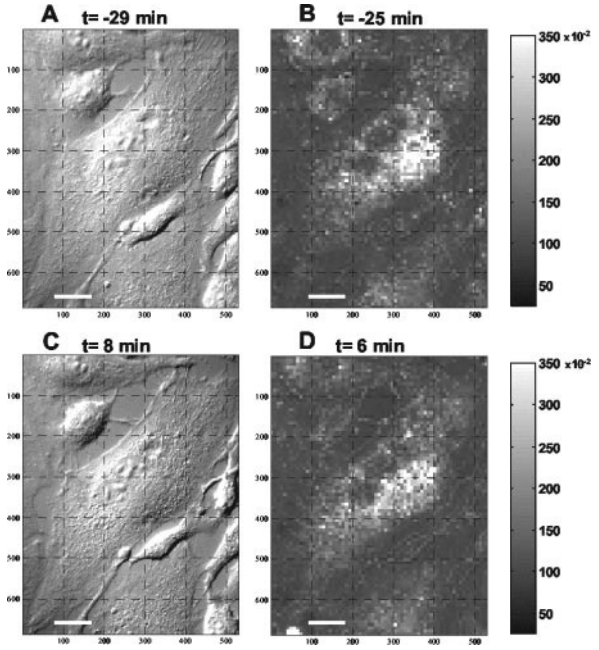

FIGURE 5 Differential interference contrast (*A* and *C*) and OSI images (*B* and *D*) of an endothelial cell subjected to calcium injury in the presence of CsA. Calcium (1.6 mM, solution 3 in Table 1 supplemented with 25 μM CsA) was added at $t = 0$ after permeabilization by ionomycin (20 μM). Scale bar, 20 μm.

Light scatter simulation of mitochondrial rounding

To assess whether the rounding of elongated scatterers does in fact result in an increase in scatter ratio, we conducted simulations of light scattering by ellipsoidal and spherical particles. Ellipsoids were used to approximate mitochondrial shape before the calcium injury; spheres were used to model the mitochondria after the injury. Based on published morphometric measurements in liver parenchymal cells (Loud ,1968), we find that the short axis of mitochondria may vary between 0.3 μm and 0.6 μm, whereas the length of the mitochondria may vary from 2 μm to as much as 11 μm. This variation in mitochondrial length was reflected in our endothelial cells. Some endothelial cells seemed to have long mitochondria (the cell in the center of the field in Fig. 2 *B*), whereas others (such as the cells adjacent to the one in the center of the field in Fig. 2 *B*) had shorter mitochondria. In addition, mitochondria may appear artificially long in certain cases where long strands may actually correspond to two shorter and overlapping mitochondria in different focal planes. In light of the difficulty in obtaining an accurate mitochondrial length estimate directly from our images, and the fact that mitochondrial width is below the resolution of our microscope, we relied on the mitochondrial measurements published by Loud to estimate the initial mitochondrial dimensions. The average short and long axes diameters of the mitochondria before the calcium insult were taken to be 0.5 μm and 4 μm, respectively. Three sphere diameters were used to model the mitochondria after the calcium overload. As shown in Table 3, upon rounding into a sphere of the same volume (case A→B), the scatter ratio increased by 10%, in close agreement with the 14% relative OSIR increase that was measured. However, if the sphere diameter keeps increasing (cases B→C→D), OSIR decreases. Thus, the modeling results suggest that OSIR increase results from a mitochondrial shape change, which consisted primarily of rounding with little volume increase, or swelling.

TABLE 3 Light scatter simulation results for ellipsoids and spheres

Simulation case	A	B	C	D	A′	A″
Refractive index ratio	1.04	1.04	1.04	1.04	1.11	1.005
Dx (μm)	4.00	1.00	1.04	1.14	4.00	4.00
Dy = *Dz* (μm)	0.50	1.00	1.04	1.14	0.50	0.50
Particle volume (μm^3)	0.52	0.52	0.59	0.78	0.52	0.52
OSIR	3.33	3.67	3.44	2.95	3.30	3.36

Dx is the long axis of the ellipsoid. *Dy* and *Dz* are the short axes. For a sphere *Dx* = *Dy* = *Dz*. The incident light was naturally polarized. The wavelength was $\lambda = 630$nm. The cytoplasm refractive index was 1.35. The initial mitochondria refractive index was 1.4 (cases A–D) and was varied to 1.5 and 1.36 (cases A′ and A″). The refractive index ratio is the ratio of mitochondria/cytoplasm index.

It is important to reemphasize that the scattering response modeled by the ellipsoid in Table 3 corresponds to an average representative case that can result in a relative OSIR increase as predicted by scatter physics. As was discussed above, the mitochondria in our experiment may have varying lengths and diameters. In general, at any given diameter between 0.3 and 0.5 μm, and up to a length of ~5 μm, our model predicts that OSIR will increase upon particle rounding at constant volume. Rounding of ellipsoids longer than 5 μm will, however, result in OSIR decrease according to our model. This is because when the length of the ellipsoid is larger than 5 μm, the angular scattering properties are already dominated by the width of the ellipsoid, and the OSIR is independent of the ellipsoid's length. Thus, at any given width between 0.3 and 0.5 μm, ellipsoids longer than 5 μm will have the same OSIR as the 5-μm-long ellipsoids, even though their volume is larger. At the same time, the OSIR will continue to decrease for spheres with corresponding increasing volumes. Thus, very long ellipsoids with high aspect ratios will typically round up into spheres with lower OSIR, whereas ellipsoids with lengths smaller than 5 μm round up into spheres with higher OSIR. Because the average OSIR increased by 14% in our study, then based on the model prediction, this increase would result from the rounding of particles that are 4–5 μm in length (for diameters between 0.3 and 0.5 μm). Based on the model, we then conclude that the mitochondria are behaving on average like 4–5-μm-long particles. This average 4–5-μm length is consistent with the observation in

our images and with the lengths of mitochondria reported in the literature.

To investigate whether changes in refractive index could account for the OSIR increase, we varied the refractive index of the initial ellipsoid (cases A′ and A″ in Table 3). The OSIR changes resulting from variations in refractive index were negligible. Although changes in mitochondrial index may have occurred as a result of the calcium overload, these changes could result only in intensity changes in the original dark-field images. In particular, a change in organelle refractive index may be responsible for the intensity increase in the initial dark-field images going from Fig. 3 *A* to Fig. 3 *D* upon calcium overload. However, the scatter predictions suggest that once the ratio of high NA to low NA signal is taken, the intensity of the ratiometric OSI images (Fig. 3, *C* and *F*) is itself insensitive to refractive index change. The theoretical predictions therefore imply that the change in OSIR is primarily caused by the mitochondrial shape change.

Fig. 6 shows the scattering intensities as a function of the angles θ and ϕ (see Eq. 1) for cases A and B in Table 3. The scattering θ-ϕ plane depicted in Fig. 6 is equivalent to a diffraction pattern. The scattering angle θ increases in the radial direction, with $\theta = 0$ corresponding to forward scatter (center of graph). The azimuthal scatter angle ϕ increases counterclockwise. In Fig. 6, the scatter intensity integral at high NA is represented by the area bound by the dashed white circle and center stop ($2° < \theta < 67°$), whereas the low NA integral is the area bound by the dotted black circle and center stop ($2° < \theta < 10°$). These high and low limits also illustrate the diameter of the variable iris in the plane F′ of the optical setup (Fig. 1). Thus, the OSIR calculated in Eq. 1 is a measure of angular scatter anisotropy in the θ direction, represented by the ratio of side to forward angle scatter intensity. Anisotropy in the ϕ direction is averaged out by integrating ϕ from 0° to 360°. For spheres, for which there is no scatter anisotropy in the ϕ direction (Fig. 6 *B*), the OSIR was previously shown to decrease monotonically for diameters D, $0.2\ \mu m < D < 1.5\ \mu m$, at 630 nm (Boustany et al., 2001). In contrast, nonspherical elongated particles exhibit both θ and ϕ anisotropy (Fig. 6 *A*). The present theoretical predictions show that particle shape change results not only in alteration in ϕ anisotropy but also in a measurable change in θ anisotropy (OSIR change between cases A and B in Table 2).

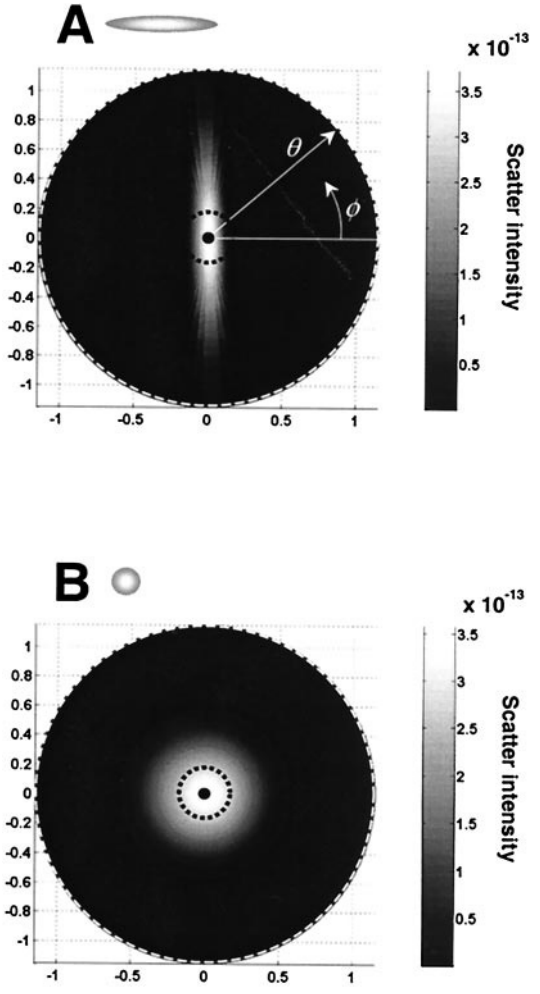

FIGURE 6 Scattering pattern predictions in the plane F′ of the optical setup for an ellipsoid and a sphere of equal volume. The black dot in the center represents the beam block at the center of the variable iris (see Fig. 1). The diameter of the dashed white circle represents the iris diameter in the high NA position; that of the dotted black circle represents the iris diameter in the low NA position. Scattering intensities (gray scale) are shown as a function of θ and ϕ for the ellipsoid and sphere in cases A and B of Table 3 (*A* and *B*, respectively). The angle of scatter θ increases radially from 0 to 1.2 radians (68.8°), with $\theta = 0$ (center of graph) representing forward scattering. The azimuthal angle of scatter ϕ increases counterclockwise going from 0° to 360°. In case A, the ellipsoid above the graph shows the orientation of the particle with respect to the θ-ϕ plane. In both panels, the incident light is propagating in the direction perpendicular to the θ-ϕ plane (into the paper).

DISCUSSION

The optical scatter imaging technique, OSI, presented here complements current microscopic methods by providing images that directly encode angular scatter data from subcellular organelles. The intensity of the ratiometric scatter images corresponds to the ratio of side-to-forward scattering intensity measured at each pixel. This scatter ratio, OSIR, correlates with subcellular morphological change. In this paper, OSIR was shown to increase within the cytoplasm of cells subjected to calcium injury. In these cells, there was a concomitant rounding of mitochondria, which appeared initially elongated. The calcium-induced mitochondrial rounding and scatter changes that ensued were suppressed by the mitochondrial permeability transition inhibitor, CsA. Thus, the measured scatter changes were directly attributable to mitochondria and the mitochondrial permeability transition. These results also suggest that the mitochondria are a sig-

nificant subcellular scatterer, and corroborate previous data underlining the large contribution of mitochondria to the scattering of biological tissue (Beauvoit et al., 1994, 1995).

Mitochondrial content may vary greatly from cell to cell (Beauvoit et al., 1995). Comparing endothelial cells with hepatocytes for example, we find that the volume fraction of mitochondria in hepatocytes is 28.3%, whereas it is only 4.3% in endothelial cells (Blouin et al., 1977). Because we have been able to successfully correlate our scatter signal with changes in mitochondrial morphology in endothelial cells, which have a relatively low mitochondrial content, we would expect that detecting changes in light scatter by mitochondria should be possible in cell types where the volume fraction of mitochondria is at least 4%. Cells with higher mitochondrial content, such as hepatocytes, would be expected to provide better mitochondrial scattering signals. It is also important to note that by being able to spatially exclude the nucleus in our analysis, we have eliminated a significant scattering component of the cell. This may explain why even though the volume fraction of mitochondria is low in endothelial cells, we can still detect a significant mitochondrial signal. Additional experimental studies are, however, necessary to show how the technique will actually work in other cell types. In particular, changes in angular scatter by certain cells could potentially originate from alterations in a highly scattering subcellular structure in addition to mitochondria. In this case, and as for this paper, attributing the OSIR changes to mitochondria will depend on proper microscopic observation, biochemical manipulation, and optical scatter modeling. Very inhomogeneous cells may also be analyzed by considering the OSIR in specific subregions of the cell, as opposed to averaging the OSIR over the whole cytoplasm as was done in our study. Conversely, the ability of the technique to detect general morphological change may make it amenable to studying biological problems involving organelles other than mitochondria.

In our system, the suppression of the scatter changes by CsA in combination with microscopic evidence served to identify the mitochondrial permeability transition as the biological process underlying our measurement. On the other hand, the theoretical simulations of light scattering from an ellipsoid rounding up served to elucidate the optical basis behind the measured increase in OSIR. The approximation of the mitochondria as ellipsoids rounding up after calcium overload resulted in predicting a relative increase in the OSIR, on the order of 10%, which was in close agreement with the relative 14% increase in OSIR that was measured in cells. In addition, the simulations showed that the calculated OSIR was not significantly sensitive to refractive index changes. This suggests that changes in OSIR can be solely attributed to changes in particle size or shape. We had previously shown that the scatter ratio is independent of refractive index for spheres with diameter D, $0.2 < D < 1.5$ (with a wavelength of 630 nm) (Boustany et al., 2001). Here, this result is extended to the case of an ellipsoid.

The approximation of mitochondria as ellipsoids rounding up into spheres in response to large calcium concentration sheds light on the angular scattering properties of a particle subjected to a sudden shape change. The current simulations of light scattering by mitochondria are consistent with experimental observation to the extent that they show that mitochondrial rounding can result in a relative OSIR increase. Nonetheless, the actual average OSIR value measured in the cell cytoplasm went from 1.47 to 1.68 (Table 2) upon mitochondrial rounding compared with the calculated OSIR values, which went from 3.33 to 3.67 for ellipsoids rounding up into spheres (case A→B in Table 3). The discrepancy in absolute OSIR values could be because of the fact that mitochondria start out like rounded cylinders rather than ellipsoids and round up into spheres of larger volume than estimated. This could result in lower OSIR values than those presently predicted. To take into account the exact level of final swelling in situ and the more subtle shape/size changes that may accompany the gross change in shape will require more elaborate models of the initial and final mitochondrial matrix geometry. Ultimately, geometrical models of the mitochondria could be refined to take into account the precise mitochondrial ultrastructure (Frey and Mannella, 2000). Simulations may also become available to predict the dark-field image of three-dimensional scatterers on a pixel-by-pixel basis (Ovryn and Izen, 2000), thus taking the imaging properties of the optical system also into account.

The mitochondrial morphological changes observed in situ in this study differ from those observed in isolated mitochondrial suspensions. Isolated mitochondria are initially spherical in shape as opposed to elongated rounded cylinders. Studies of the mitochondrial permeability transition in isolated mitochondria do not show rounding of the mitochondria from an initially elongated shape. Instead, the mitochondrial permeability transition in isolated mitochondria is typically accompanied by swelling of the spherically shaped mitochondria and transition from an initial aggregated matrix state to the noncondensed orthodox matrix configuration (Hunter et al., 1976; Pfeiffer et al., 1976; Beatrice et al., 1984; Petronilli et al., 1993). One exception is the study by Reed and Savage (1995) who show that CsA-dependent permeabilization of the mitochondrial inner membrane can be achieved with or without swelling of isolated liver mitochondria. Still in that study, the mitochondria are initially spherical. Thus, the cytoplasmic environment and the presence of cytoskeletal proteins may play an important role in maintaining the shape of mitochondria in situ. One study shows in situ calcium-induced mitochondrial rounding from an initial rod-like cylindrical shape, in agreement with our observation of significant shape change (Kristal and Dubinsky, 1997). Nevertheless, in that study of mitochondria in cultured astrocytes, the rounded mitochon-

dria are reportedly swollen after calcium injury, with a final diameter exceeding their initial measured length. This very large amplitude swelling, which may accompany the shape change, was not present in our experiments (see Fig. 2). Additional studies will be necessary to assess how cell type and the cytoplasmic environment may affect the morphological nature of the mitochondrial permeability transition as observed in situ.

In this investigation, our transmission microscope was set up in the central dark-ground configuration, and wide and narrow angles of scatter were selected by varying the diameter of the aperture in a Fourier plane conjugate to the objective's back focal plane. The measured scatter ratio, OSIR, represented the wide-to-narrow scatter intensity as an indicator of particle size/shape and was directly mapped onto the full field of view. As depicted in Fig. 6, OSIR is a measure of scatter anisotropy in the θ direction. Previous scattering studies of mitochondrial suspensions have used the measurement of light transmission (or absorbance) or 90° scatter intensity to track changes in mitochondrial volume. Although under certain conditions, these measurements correlate well with mitochondrial morphology (Hunter and Haworth, 1979, Pfeiffer et al., 1976; Petronilli et al., 1993), they could present some shortcomings. The general relationship between transmitted light or light scattered at one single angle and particle volume is not always monotonic (Bryant et al., 1969; Latimer and Pyle, 1972). Moreover, changes in refractive index also contribute to the change in light scatter in addition to morphology change, thus confounding data interpretation. A study by Knight et al. (1981) shows how changes in light scattered at 90° may not necessarily correlate with mitochondrial volume change and points at the difficulty in interpreting single-angle scatter data. By comparison, the OSIR measured in this study has the advantage of decreasing monotonically over a large range of sphere diameters from 0.2 μm to 1.5 μm (see Boustany et al., 2001). Moreover, the OSIR is not significantly sensitive to refractive index changes for spheres in this size range as well as for ellipsoids with dimensions comparable to those of mitochondria in situ.

In the present setup, the scatter intensity was averaged in the azimuthal scatter direction ϕ. Scatter anisotropy in the ϕ direction may give information about particle shape for nonspherical particles and could be measured by redesigning the iris to take the ratio of two perpendicular scatter directions, such as horizontal to vertical scatter with respect to the θ-ϕ plane. This ratio would be a function of the particle orientation with respect to the optical axis. To provide particle shape anisotropy, the iris will need to be rotated in the ϕ direction while several ratiometric images are collected and later processed. Alternatively, particle shape and orientation may be probed by varying the polarization of the incident beam. In general, our method consists of directly mapping selective scatter information into the imaging plane by use of a spatial filter in the Fourier plane. Although we have chosen to first look at the ratio of wide-to-narrow-angle scatter, other Fourier plane apertures could easily be designed to select different scattering parameters.

To date, most light-scatter-based studies on mitochondrial morphology have been conducted in preparations of isolated mitochondria. Although studies on the mitochondrial permeability transition can now be conducted in situ by observing the movement of the fluorescent dye calcein-AM across the mitochondrial inner membrane (Lemasters et al., 1998; Petronilli et al., 1999), changes in the actual morphology of mitochondria have rarely been directly assessed from an optical measurement made in situ. One example is the study by Kristal and Dubinsky (1997), where mitochondria in cultured cortical astrocytes are classified according to their shape (rod-like or rounded) and counted after labeling with the fluorescent dye JC1. Another is the study of mitochondrial volume in situ using measurements of light scattering by hepatocytes in suspension (Quinlan et al., 1983). As shown in Fig. 2, large amplitude mitochondrial shape changes could be detected by differential interference contrast (DIC) and fluorescence. However, to quantify the observed changes, one would have to analyze the DIC and fluorescence images in great detail. OSI gives a rapid quantification of the data. The particles being probed need not be individually resolved and measured by traditional morphometric methods, thus avoiding a tedious process of image recognition, particle sizing, and counting. OSI complements current microscopic methods, allows real-time monitoring of the same cells, and could be easily automated and extended to high-throughput screening.

We thank Prof. Rebecca Richards-Kortum from the University of Texas, Austin, for graciously giving a copy of the finite-difference time-domain software developed in her laboratory.

This work was supported by National Institutes of Health grant R21-RR15264. N.N.B. was also partially supported by a fellowship from the Whitaker foundation.

REFERENCES

Beatrice, M. C., D. L. Stiers, and D. R. Pfeiffer. 1984. The role of glutathione in the retention of Ca^{2+} by liver mitochondria. *J. Biol. Chem.* 259:1279–1287.

Beauvoit, B., S. M. Evans, T. W. Jenkins, E. E. Miller, and B. Chance. 1995. Correlation between the light scattering and the mitochondrial content of normal tissues and transplantable rodent tumors. *Anal. Biochem.* 226:167–174.

Beauvoit, B., T. Kitai, and B. Chance. 1994. Contribution of the mitochondrial compartment to the optical properties of the rat liver: a theoretical and practical approach. *Biophys. J.* 67:2501–2510.

Bernardi, P. 1992. Modulation of the mitochondrial cyclosporin A-sensitive permeability transition pore by the proton electrochemical gradient. *J. Biol. Chem.* 267:8834–8839.

Bernardi, P., V. Petronilli, F. D. Lisa, and M. Forte. 2001. A mitochondrial perspective on cell death. *Trends Biochem. Sci.* 26:112–117.

Bernardi, P., S. Vassanelli, P. Veronese, R. Colonna, I. Szabo, and M. Zoratti. 1992. Modulation of the mitochondrial permeability transition pore. *J. Biol. Chem.* 267:2934–2939.

Blouin, A., R. P. Bolender, and E. R. Weibel. 1977. Distribution of organelles and membranes between hepatocytes and nonhepatocytes in the rat liver parenchyma. *J. Cell Biol.* 72:441–445.

Boustany, N. N., S. C. Kuo, and N. V. Thakor. 2001. Optical scatter imaging: subcellular morphometry in situ with Fourier filtering. *Optics Lett.* 26:1063–1065.

Broekemeier, K. M., M. E. Dempsey, and D. R. Pfeiffer. 1989. Cyclosporin A is a potent inhibitor of the inner membrane permeability transition in liver mitochondria. *J. Biol. Chem.* 264:7826–7830.

Bryant, F. D., P. Latimer, and B. A. Seiber. 1969. Changes in total light scattering and absorption caused by changes in particle conformation: a test of theory. *Arch. Biochem. Biophys.* 135:109–117.

Constantini, P., B. V. Chernyak, V. Petronilli, and P. Bernardi. 1996. Modulation of the mitochondrial permeability transition pore by pyridine nucleotides and dithiol oxidation at two separate sites. *J. Biol. Chem.* 271:6746–6751.

DiLisa, F., R. Menabo, M. Canton, and V. Petronilli. 1998. The role of mitochondria in the salvage and the injury if the ischemic myocardium. *Biochim. Biophys. Acta.* 1366:69–78.

Drezek, R., A. Dunn, and R. Richards-Kortum. 1999. Light scattering from cells: finite-difference time-domain simulations and goniometric measurements. *Appl. Optics.* 38:3651–3661.

Dunn, A., and R. Richards-Kortum. 1996. Three-dimensional computation of light scattering from cells. *IEEE J. Select. Topics Quant. Electron.* 2:898–905.

Finucane, D. M., E. Bossy-Wetzel, N. J. Waterhouse, T. G. Cotter, and D. R. Green. 1999. Bax-induced caspase activation and apoptosis via cytochrome c release from mitochondria is inhibitable by Bcl-xL. *J. Biol. Chem.* 274:2225–2233.

Frey, T. G., and C. A. Mannella. 2000. The internal structure of mitochondria. *Trends Biol. Sci.* 25:319–324.

Hackenbrock, C. R. 1966. Ultrastructural bases for metabolically linked mechanical acivity in mitochondria I. *J. Cell Biol.* 30:269–297.

Halestrap, A. P. 1994. Regulation of mitochondrial metabolism through changes in matrix volume. *Biochem. Soc. Trans.* 22:522–529.

Harris, R. A., M. A. Asbell, J. Asai, W. W. Jolly, and D. E. Green. 1969. The conformational basis of energy transduction in membrane systems. V. Measurement of configurational changes by light scattering. *Arch. Biochem. Biophys.* 132:545–560.

Herdson, P. B., H. M. Sommers, and R. B. Jennings. 1964. A comparative study of the fine structure of normal and ischemic dog myocardium with special reference to early changes following temporary occlusion of a coronary artery. *Am. J. Pathol.* 46:367–386.

Hoek, J. B., J. L. Farber, A. P. Thomas, and X. Wang. 1995. Calcium ion-dependent signaling and mitochondrial dysfunction: mitochondrial calcium uptake during hormonal stimulation in intact liver cells and its implication for the mitochondrial permeability transition. *Biochim. Biophys. Acta.* 1271:93–102.

Hunter, D. R., and R. A. Haworth. 1979. The Ca^{2+}-induced membrane transition in mitochondria. *Arch. Biochem. Biophys.* 195:453–459.

Hunter, D. R., R. A. Haworth, and J. H. Southward. 1976. Relationship between configuration, function, and permeability in calcium-treated mitochondria. *J. Biol. Chem.* 251:5069–5077.

Jurgensmeier, J. M., Z. Xie, Q. Deveraux, L. Ellerby, D. Bredesen, and J. C. Reed. 1998. Bax directly induces release of cytochrome c from isolated mitochondria. *Proc. Natl. Acad. Sci. U.S.A.* 95:4997–5002.

Knight, V. A., P. M. Wiggins, J. D. Harvey, and J. A. O'Brien. 1981. The relationship between the size of mitochondria and the intensity of light that they scatter in different states. *Biochim. Biophys. Acta.* 637: 146–151.

Kristal, B. S., and J. M. Dubinsky. 1997. Mitochondrial permeability transition in the central nervous system: induction by calcium cycling-dependent and -independent pathways. *J. Neurochem.* 69:524–538.

Latimer, P., and B. E. Pyle. 1972. Light scattering at various angles: theoretical predictions of the effects of particle volume change. *Biophys. J.* 12:764–773.

Lehninger, A. L. 1959. Reversal of thyroxine-induced swelling of rat liver mitochondria by adenosine triphosphate. *J. Biol. Chem.* 234: 2187–2195.

Lemasters, J. J., A-L. Nieminen, T. Qian, L. C. Trost, S. P. Elmore, Y. Nishimura, R. A. Crowe, W. E. Cascio, C. A. Bradham, D. A. Brenner, and B. Herman. 1998. The mitochondrial permeability transition in cell death: a common mechanism in necrosis, apoptosis and autophagy. *Biochim. Biophys. Acta.* 1366:177–196.

Lewis, J. M., M. J. Woolkalis, G. L. Gerton, R. M. Smith, L. Jarett, and D. Manning. 1991. Subcellular distribution of the alpha subunit(s) of Gi: visualization by immunofluorescent and immunological labeling. *Cell Regul.* 2:1097–1113.

Loud, A. V. 1968. A quantitative stereological description of the ultrastructure of normal rat liver parenchymal cells. *J. Cell Biol.* 37:27–46.

Martinou, I., S. Desagher, R. Eskes, B. Antonsson, E. Andre, S. Fakan, and J-C. Martinou. 1999. The release of cytochrome c from mitochondria during apoptosis of NGF-deprived sympathetic neurons is a reversible event. *J. Cell Biol.* 144:883–889.

Mootha, V. K., M. C. Wei, K. F. Buttle, L. Scorrano, V. Panoutsakopoulou, C. A. Mannella, and S. J. Korsmeyer. 2001. A reversible component of mitochondrial respiratory dysfunction in apoptosis can be rescued by exogenous cytochrome c. *EMBO J.* 20:661–671.

Narita, M., S. Shimizu, T. Ito, T. Chittenden, R. J. Lutz, H. Matsuda, and Y. Tsujimoto. 1998. Bax interacts with the permeability transition pore to induce permeability transition and cytochrome c release in isolated mitochondria. *Proc. Natl. Acad. Sci. U.S.A.* 95:14681–14686.

Ovryn, B., and S. H. Izen. 2000. Imaging of transparent spheres through a planar interface using a high-numerical-aperture optical microscope. *J. Optic. Soc. Am. A.* 17:1202–1213.

Packer, L. 1960. Metabolic and structural states of mitochondria. *J. Biol. Chem.* 235:242–249.

Packer, L. 1967. Energy-linked low amplitude mitochondrial swelling. *Methods Enzymol.* 10:685–697.

Pastorino, J. G., J. W. Snyder, J. B. Hoek, and J. L. Farber. 1995. Ca^{2+} depletion prevents anoxic death of hepatocytes by inhibiting mitochondrial permeability transition. *Am. J. Physiol.* 268:C676–C685.

Petronilli, V., C. Cola, S. Massari, R. Colonna, and P. Bernardi. 1993. Physiological effectors modify voltage sensing by the cyclosporin A-sensitive permeability transition pore of mitochondria. *J. Biol. Chem.* 268:21939–21945.

Petronilli, V., P. Constantini, L. Scorrano, R. Colonna, S. Passamonti, and P. Bernardi. 1994. The voltage sensor of the mitochondrial permeability transition pore is tuned by the oxidation-reduction state of vicinal thiols. *J. Biol. Chem.* 269:16638–16642.

Petronilli, V., G. Miotto, M. Canton, M. Brini, R. Colonna, and P. Bernardi. 1999. Transient and long-lasting openings of the mitochondrial permeability transition pore can be monitored directly in intact cells by changes in mitochondrial calcein fluorescence. *Biophys. J.* 76:725–734.

Pfeiffer, D. R., T. H. Kuo, and T. T. Chen. 1976. Some Effect of Ca^{2+}, Mg^{2+}, and Mn^{2+} on the ultrastructure, light scattering properties, and malic enzyme activity of adrenal cortex mitochondria. *Arch. Biochem. Biophys.* 176:556–563.

Quinlan, P. T., A. P. Thomas, A. E. Armston, and A. P. Halestrap. 1983. Measurement of intramitochondrial volume in hepatocytes without cell disruption and its elevation by hormones and valinomycin. *Biochem. J.* 214:395–404.

Reed, D. J., and M. K. Savage. 1995. Influence of metabolic inhibitors on mitochondrial permeability transition and glutathione status. *Biochim. Biophys. Acta.* 1271:43–50.

Scorrano, L., M. Ashiya, K. Buttle, S. Weiler, S. A. Oakes, C. A. Mannella, and S. J. Korsmeyer. 2002. A distinct pathway remodels mitochondrial cristae and mobilizes cytochrome c during apoptosis. *Dev. Cell.* 2:55–67.

Scorrano, L., V. Petronilli, and P. Bernardi. 1997. On the voltage dependence of the mitochondrial permeability transition pore. *J. Biol. Chem.* 272:12295–12299.

Siemens, A., R. Walter, L-H. Liaw, and M. W. Berns. 1982. Laser-stimulated fluorescence of submicrometer regions within single mitochondria of rhodamine-treated cells in culture. *Proc. Natl. Acad. Sci. U.S.A.* 79:466–470.

Steinberg, S. F., J. O. Bilezikian, and Q. Al-Awqati. 1987. Fura-2 fluorescence is localized to mitochondria in endothelial cells. *Am. J. Physiol.* 253:C744–C747.

Territo, P. R., S. A. French, M. C. Dunleavy, F. J. Evans, and R. S. Balaban. 2001. Calcium activation of heart mitochondrial oxidative phosphorylation. *J. Biol. Chem.* 276:2586–2599.

Vander-Heiden, M. G., N. S. Chandel, E. K. Williamson, P. T. Schumacker, and C. B. Thompson. 1997. Bcl-xL regulates the membrane potential and volume homeostasis of mitochondria. *Cell.* 91: 627–637.

Zamzami, N., S. A. Susin, P. Marchetti, T. Hirsh, I. Gomez-Monterrey, M. Castedo, and G. Kroemer. 1996. Mitochondrial control of apoptosis. *J. Exp. Med.* 183:1533–1544.

Zoratti, M., and I. Szabo. 1995. The mitochondrial permeability transition. *Biochim. Biophys. Acta.* 1241:139–176.